Research
Biochemical Engineering—Article

# Fully Superhydrophilic, Self-Floatable, and Multi-Contamination-Resistant Solar Steam Generator Inspired by Seaweed

Chiyu Wen [a,#], Hongshuang Guo [a,#], Yingnan Zhu [a], Haoyu Bai [b,c], Weiqiang Zhao [a], Xinsheng Wang [b,c], Jing Yang [a], Moyuan Cao [b,c,*], Lei Zhang [a,*]

[a] Frontier Science Center for Synthetic Biology & Key Laboratory of Systems Bioengineering (Ministry of Education), Department of Biochemical Engineering, School of Chemical Engineering and Technology, Tianjin University, Tianjin 300072, China
[b] Haihe Laboratory of Sustainable Chemical Transformations, School of Materials Science and Engineering, Nankai University, Tianjin 300071, China
[c] State Key Laboratory of Chemical Engineering, School of Chemical Engineering and Technology, Tianjin University, Tianjin 300072, China

## ARTICLE INFO

## ABSTRACT

Highly hydrophilic materials enable rapid water delivery and salt redissolution in solar-driven seawater desalination. However, the lack of independent floatability inhibits heat localization at the air/water interface. In nature, seaweeds with internal gas microvesicles can float near the sea surface to ensure photosynthesis. Here, we have developed a seaweed-inspired, independently floatable, but superhydrophilic (SIFS) solar evaporator. It needs no extra floatation support and can simultaneously achieve continuous water pumping and heat concentration. The evaporator resists salt accumulation, oil pollution, microbial corrosion, and protein adsorption. Densely packed hollow glass microbeads promote intrinsic floatability and heat insulation. Superhydrophilic zwitterionic sulfobetaine hydrogel provides a continuous water supply, redissolves the deposited salt, and endows the SIFS evaporator with excellent anti-fouling properties. With its unprecedented anti-contamination ability, this SIFS evaporator is expected to open a new avenue for designing floatable superhydrophilic materials and solving real-world issues of solar steam generation in complex environmental conditions.

© 2022 THE AUTHORS. Published by Elsevier LTD on behalf of Chinese Academy of Engineering and Higher Education Press Limited Company. This is an open access article under the CC BY-NC-ND license (http://creativecommons.org/licenses/by-nc-nd/4.0/).

## 1. Introduction

With the expanding global population, booming industrial manufacturing, and aggravated water pollution, the energy crisis and freshwater scarcity have become two of the most urgent issues worldwide [1–7]. Solar energy is an inexhaustible and environmentally friendly resource, and the ocean provides an abundant supply of water. Consequently, concentrating solar irradiation to distill seawater into freshwater is a sustainable approach for fulfilling the ever-increasing demands of humans [8–11]. Compared to bulk water heating, interfacial heating localizes the incident energy where evaporation occurs and limits the heat loss, thereby boosting the photothermal conversion efficiency [12,13]. Therefore, interfacial solar desalination has been proposed as a superior option for long-term freshwater production without the extensive use of equipment and consumption of energy [14–16].

The major breakthroughs in highly efficient solar-to-steam conversion have been developed based on novel photothermal materials such as carbon nanotubes, graphene oxide, polypyrrole, and carbonized biomass, as well as innovative structural designs [17–26]. However, as the ocean is a complex system, the long-term stability and robustness of interfacial solar evaporators are still limited by the following issues in real-world applications [27–30]: ① Salt deposition developing from seawater evaporation is likely to block the water transport channels [31,32]; ② oil spillage occurs occasionally, and oil pollution on the evaporator can reduce the water evaporation rate and shorten its working life; ③ numerous microbes live in the ocean, and the occurrence and development of microbial adhesion may cause subsequent clogging and corrosion of evaporators [33]; ④ extreme weather conditions, such as storm events, may produce violent winds and waves, resulting in lashing and tearing of the evaporator; ⑤ solar flux inputs energy into the evaporator, leading to high surface temperature of photothermal materials [34].

---

In light of these challenges, efforts have been made in the past decades to exploit, develop, and optimize solar interfacial desalination systems [35–39]. In previous studies, designing hydrophobic surfaces or utilizing additional supporting structures have been widely used to support the desalination system at the air/water interface [40–43]. However, these hydrophobic surfaces and supports may increase the risk of evaporator contamination and microplastics discharge, potentially decreasing the longevity of the evaporators and harming the environment [44].

Localizing solar-thermal heat generation at the air/water interface is the key to achieving a high photothermal conversion efficiency and evaporation rate [45,46]. However, superhydrophilicity and self-floatability are contradictory properties. Normally, a fully superhydrophilic device cannot float independently because it is likely to be completely wetted and to reach a density similar to or even higher than that of water, thereby sinking to the bottom. However, humans can learn much from nature. In the ocean, seaweeds possess a superhydrophilic surface and succulent interior, but numerous species are still able to float near the sea surface and perform photosynthesis for survival [47]. Gas-vesicle structures in cells contribute to the low density of these seaweeds [48]. Several gas vesicles aggregate to form compound gas vacuoles, which display variable shapes and sizes in different species [49]. The gas-vesicle structures endow the seaweeds with light weight and independent floatability. Here, we have applied this type of hollow structure to a zwitterionic hydrogel to enable independent floating and interfacial solar steam generation [50].

In this study, we have developed a seaweed-inspired independently floatable but superhydrophilic (SIFS) solar steam generator that possesses broadband light absorption, heat insulation, independent and detachable floatability, salt rejection, oil repellence, biofouling resistance, highly efficient water evaporation, and long-term stability. Low-cost carbon black (CB) is dispersed throughout the evaporator to achieve a broadband solar absorption of 96.35%. Densely packed hollow glass microbeads (HGBs) allow it to float at the sea surface and perform interfacial steam generation. Zwitterionic sulfobetaine (ZSB) hydrogel is employed as an adhesive and antifouling coating. Superhydrophilic ZSB possesses a high degree of wettability to provide continuous water pumping; consequently, salt can be simply dissolved instead of being deposited as a solid on the evaporator [51]. Moreover, the ZSB hydrogel binds a large amount of water molecules to form a hydration layer, protecting the evaporator from direct contact with the oil- and biofoulants [52,53]. Compared to the commonly used polystyrene foam (PS-f), the SIFS evaporator possesses a sharply reduced degree of adhesion (> 97%) by both *Escherichia coli* (*E. coli*) and *Staphylococcus aureus* (*S. aureus*). Under one sun illumination, the floater produced a photothermal conversion efficiency of 63.27% and a steam generation rate of 1.35 kg·m$^{-2}$·h$^{-1}$. The floater can maintain its intact structure and surface cleaning over 30 days in artificial seawater and wastewater, indicating a durable and stable performance. This seaweed-inspired evaporator provides facile and practical access to freshwater production in complex environments, paving the way for solar-driven distillation from seawater or even wastewater.

## 2. Experimental section

### 2.1. Materials

The zwitterionic sulfobetaine (95%), *N,N*′-methylene bisacrylamide (MBAA, 99%), and ammonium persulfate (APS, 99%) were purchased from Sigma (USA). CB was obtained from Degussa (Germany). 2-Hydroxy-2-methyl-propiophenone (HMPF, 98%)

was obtained from Adamas (China). Hollow glass microbeads with an average diameter of 100 μm were purchased from Minnesota Mining and Manufacturing Corporation (USA). The crude oil was sponsored by the China National Offshore Oil Corporation. All deionized water (DI) used in this work was purified using a Millipore purification system (Millipore, Ltd., USA).

### 2.2. Preparation of the SIFS solar evaporator

To fabricate the SIFS solar evaporator, ZSB (2.232 g, 8 mmol) monomer, MBAA (6.28 mg, 0.04 mmol) crosslinker, and APS (4 mg, 0.017 mmol) thermal initiator were dissolved in DI (2 mL) to prepare the pre-gel solution. A moderate amount of HGBs was added to the pre-gel solution, followed by thorough mixing. After standing for 30 min at 4 °C, the floating HGBs (1 g) were collected and stirred with CB (40 mg) and poured into a polytetrafluoroethylene (PTFE) mold, followed by thermal crosslinking at 37 °C for 4 h to obtain the SIFS evaporator. Pure ZSB hydrogel and ZSB hydrogel only packed with HGBs (ZSB/G) were also prepared as controls.

### 2.3. Solar steam generation of the SIFS evaporator

ZSB/G and SIFS samples with an area of 1 cm × 1 cm and different thicknesses (1, 2, 3, 4, and 5 mm) were used for the solar steam generation tests. The sample was floated in a transparent cuvette filled with artificial seawater. A solar simulator with an air mass 1.5 global (AM 1.5G) light filter and a xenon lamp was employed to provide sunlight at a density of 1 kW·m$^{-2}$ (1 sun). The light density was monitored and adjusted using a solar power meter (SM206, Xinbao, China). The change in water mass of each sample was measured every 30 min. A thermal infrared camera was used to collect infrared images.

### 2.4. Antifouling properties of the SIFS evaporator

The antifouling properties of the SIFS evaporator were evaluated by adhesion assays with protein, bacteria, and oil (soybean oil and crude oil), and salt rejection tests.

For the protein contamination test, fluorescein isothiocyanate (FITC)-labeled bovine serum albumin (FITC-BSA) was selected as the model protein. FITC provided a fluorescence signal that was captured by a fluorescence microscope, so that the protein adhesion could be measured and normalized via fluorescence intensity. All the test samples were washed with 0.9% NaCl solution before the test. The samples were then co-incubated with FITC-BSA (0.5 mg·mL$^{-1}$) for 30 min in the dark. After gently washing three times with 0.9% NaCl, the fluorescence signal was observed using an inverted fluorescence microscope (Ti-S, Nikon Eclipse, Japan). The relative fluorescence intensities were normalized to the area of the observed sample using the ImageJ software.

In the bacterial adhesion test, *E. coli* and *S. aureus* were seeded and cultured in Luria–Bertani (LB) medium overnight, respectively. Sterile samples were incubated with 1 mL bacterial diluent (1 × 10$^7$ cells·mL$^{-1}$) at 37 °C for 2 h, followed by gentle washing with 0.9% NaCl to remove the insufficiently adhering bacteria. Then, the samples were immersed in 0.9% NaCl, and intermittent ultrasonication was applied to peel off the tightly adhering bacteria without damage. The suspension was removed to spread the LB agar culture medium plate. After overnight cultivation, the number of bacterial colonies on the plates was recorded to evaluate the anti-bacterial properties. In addition, the test samples were co-cultured with *E. coli* for 3 d at a concentration of 1 × 10$^9$ cells·mL$^{-1}$. Bacterial attachment and reproduction on the surface were observed using scanning electron microscope (SEM, Merlin Compact, Zeiss, Germany).

ZSB/G was employed to conduct an anti-oil test for better visual perception of oil removal. The test samples were completely immersed in crude oil or red-labelled soybean oil, and then the samples were rinsed with DI. Optical images were collected for oil repellence and self-cleaning.

The salt rejection of the SIFS evaporator was evaluated via salt dissolution, degradation, and absorption tests. The dissolution experiment was conducted using a glass beaker with 3.6 wt% NaCl aqueous solution. An SIFS hydrogel was floated in a beaker with manually applied salt, and a camera was used to periodically photograph the salt dissolving over the course of the test [37].

In the salt degradation assay, samples were dried at 60 °C for 48 h to a mass of $m_1$. Then, the hydrogels were degraded in artificial seawater or DI for 2 h, followed by full washing and swelling in DI water to a mass of $m_2$. Subsequently, the samples were dried again at 60 °C prior to the next cycle [63]. Five cycles were applied to all the hydrogels. The swelling ratio $R$ of the hydrogels can be mathematically expressed as Eq. (1):

$$R = \frac{m_2}{m_1} \tag{1}$$

In the salt absorption assay, the test samples were dried at 60 °C for 48 h to a mass of $m_3$. Then the samples were fully swelled in 3.6 wt% NaCl solution for 24 h to a mass of $m_4$. The hydrogels were dried at 60 °C for 3 d to a constant weight $m_5$, which included both the weight of the hydrogel and the absorbed NaCl. The salt rejection ratio $\varphi$ was calculated according to Eq. (2) [62]:

$$\varphi = 1 - \frac{m_5 - m_3}{0.036 \, (m_4 - m_3)} \tag{2}$$

In addition, long-term salt rejection and durability in practical applications were measured via 30 h 3.6 wt% NaCl solution desalination.

## 3. Results and discussion

### 3.1. Design and fabrication of SIFS evaporator

Certain seaweeds float near the sea surface to harvest sufficient solar energy for photosynthesis and metabolism. The mechanism by which hydrophilic seaweeds maintain floatability is that numerous gas microvesicles are distributed in their infrastructure to reduce the total density. Inspired by the pneumatocyst structure of these seaweeds, we selected HGBs to realize independent floatability for an superhydrophilic monolith (Fig. 1 and Appendix A Fig. S1). An antifouling ZSB hydrogel was applied to construct the bulk structure of the evaporator, and CB nanoparticles that exhibit broadband solar absorption endowed the hydrogel with an enhanced photothermal effect. An SIFS solar evaporator composed of a ZSB hydrogel monolith, HGB-based gas vesicles, and CB light absorbent material was successfully fabricated. For comparison, a pure ZSB hydrogel and a ZSB/G were also prepared and tested in the following experiments.

The chemical properties of ZSB, ZSB/G, and SIFS were evaluated via Fourier transform infrared (FTIR; Alpha II, Bruker, Germany) spectroscopy and X-ray photoelectron spectroscopy (XPS; ESCALAB 250Xi, Thermo Scientific, USA). In the FTIR spectra (Fig. S2 in Appendix A), the peaks at 1465 and 1074 cm$^{-1}$ can be ascribed to the $-N(CH_3)_2{}^+-$ and $-SO_3{}^-$ functional groups in ZSB, ZSB/G, and SIFS [54]. The signal at 1094 cm$^{-1}$ was due to the Si–O–Si bridges, and the shoulder peak at 1192 cm$^{-1}$ was attributed to the asymmetric stretching of Si–O–Si. The peak at 806 cm$^{-1}$ could be assigned to the symmetric stretching of Si–O–Si [55,56]. In the XPS spectra (Fig. S3 in Appendix A), the peaks at 102, 168, and 402 eV (1 eV = $1.602176 \times 10^{-19}$ J) corresponded to Si, S, and N elements, respectively, in SIFS and ZSB/G, while no obvious signals of Si were detected in ZSB. All the XPS spectra were calibrated with respect to the C 1s peak at 284.8 eV.

The density of fully wetted SIFS floater was ~0.72 g·cm$^{-3}$ (~0.42 g·cm$^{-3}$ for dry SIFS sample), enabling reliable floatability of the hydrogel (Fig. S4(a) in Appendix A). Compared to the pure ZSB hydrogel, the rigidity of the SIFS floater was increased by 3.56 times with a compression modulus of 0.41 MPa (Fig. S5 in Appendix A). Thus, the lightweight SIFS floater with a low density could even stand on a dandelion, and its high toughness allowed it to support a 1 kg weight without any collapse (Figs. S4(b) and (c) in Appendix A). These superior mechanical properties should guarantee floater stability in harsh and complex environments.

Similar to the natural seaweeds, the SIFS floater coated with ZSB hydrogel possessed typical superhydrophilicity and underwater superoleophobicity (Figs. 1(b) and (d), Fig. S6 and Videos S1 and S2 in Appendix A) [57]. ZSB materials have strongly charged groups, $-SO_3{}^-$ and $-N(CH_3)_2{}^+-$, to bind abundant water molecules via ionic solvation effects. These water molecules surround ZSB in dynamic equilibrium and form a hydration layer that exhibits superhydrophilicity [58]. This hydration shell also acted as a barrier to protect the SIFS hydrogel from various foulants (Fig. 1(e)). Meanwhile, the interspace between HGBs connected into channels inside the SIFS floater (Fig. 1(c) and Appendix A Fig. S7), ensuring high efficiency and continuous water transport.

Further investigation of the thermal insulation of the SIFS evaporator could reveal its heat managing ability and provide an optimal design. Based on a hot-disk method, the thermal conductivity of the pure ZSB hydrogel was assessed as 0.47 W·m$^{-1}$·K$^{-1}$. After HGBs doping, the air (0.03 W·m$^{-1}$·K$^{-1}$) stored in HGBs worked as a heat insulator to endow the ZSB/G and SIFS hydrogels with better heat insulation performance [11], corresponding to a significantly reduced thermal conductivity of 0.28 W·m$^{-1}$·K$^{-1}$, which was much lower than that of water (0.6 W·m$^{-1}$·K$^{-1}$) [59]. Therefore, because of the lower thermal conductivity induced heat insulation, the SIFS floater was able to localize heat at the air/water interface and reduce energy loss to the bulk water [60].

### 3.2. Independent and detachable floatability

Benefitting from the HGBs, a lightweight SIFS evaporator was able to stably float on the water to perform interfacial steam generation, even after 20 cycles of squeezing and releasing (Fig. 2(a), Video S3 in Appendix A). More importantly, the SIFS evaporator exhibited intrinsic floatability, that is, regardless of how broken the evaporator was, it still floated at the air/water interface automatically (Fig. 2(b), Video S4 in Appendix A). This demonstrates that the inherent independent floatability of the SIFS evaporator does not rely on the entire structure, but each part of it could float on the water and generate steam under solar irradiation.

To evaluate the stability and robustness of the SIFS evaporator, various treatments were applied. SIFS sheets were subjected to a series of treatments for 1 h each, including boiling, ultrasonication, acidic, and alkali treatments, respectively (Fig. 2(c)). After these treatments, the SIFS evaporators maintained an intact structure, and no leakage or degradation was observed. This result indicates that the SIFS evaporator possesses excellent environmental stability, which is essential for achieving long-term durability in complex real-world applications.

The measured water diffusivity of the SIFS hydrogel was compared with that of the ZSB and ZSB/G hydrogels (Figs. 2(d) and (e)). Dry samples were completely immersed in 3.6 wt% NaCl to perform the water uptake test, and the initial weight and mass change of the samples were recorded over time. The water absorption performance of the SIFS hydrogel is given by Eq. (3) [61]:
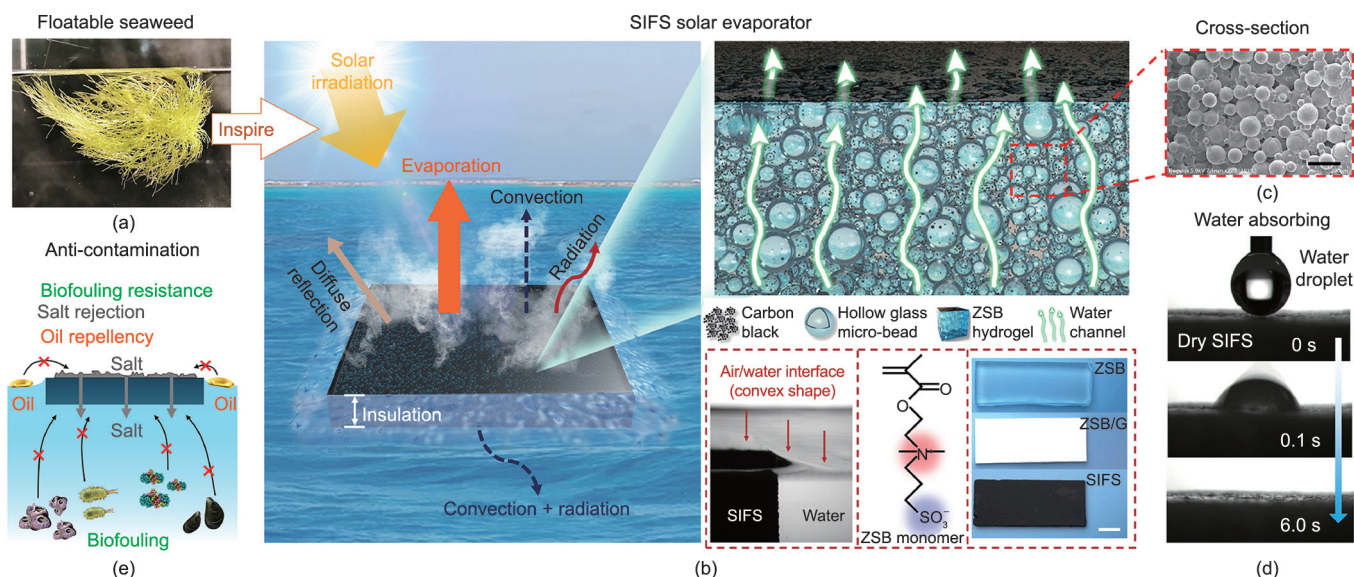
**Fig. 1.** Schematic illustration and surface characterization of the SIFS evaporator. (a) Seaweed-inspired gas vesicle for the reliable floatability of a fully superhydrophilic structure. (b) Superhydrophilic hydrogel and sunlight-absorbing material enable collective self-floatation, multi-contamination resistance, broadband solar absorption, and continuous steam generation. The molecular structure of ZSB monomer, the optical images of ZSB, ZSB/G, and SIFS hydrogels are shown at the bottom (scale bar: 1 cm). The water film on floating SIFS evaporator is connected to bulk water, forming a convex shape of air/water interface. (c) Cross-section of SIFS hydrogel, the HGBs are densely adhered by ZSB hydrogel (scale bar: 100 μm). (d) Superhydrophilicity of SIFS sample, a water droplet can be rapidly captured by dry SIFS hydrogel, indicating its high water affinity. (e) Ionic solvation effect-induced hydration layer endows SIFS evaporator with multi-contamination resistance, e.g., biofouling resistance, salt rejection, and oil repellence.
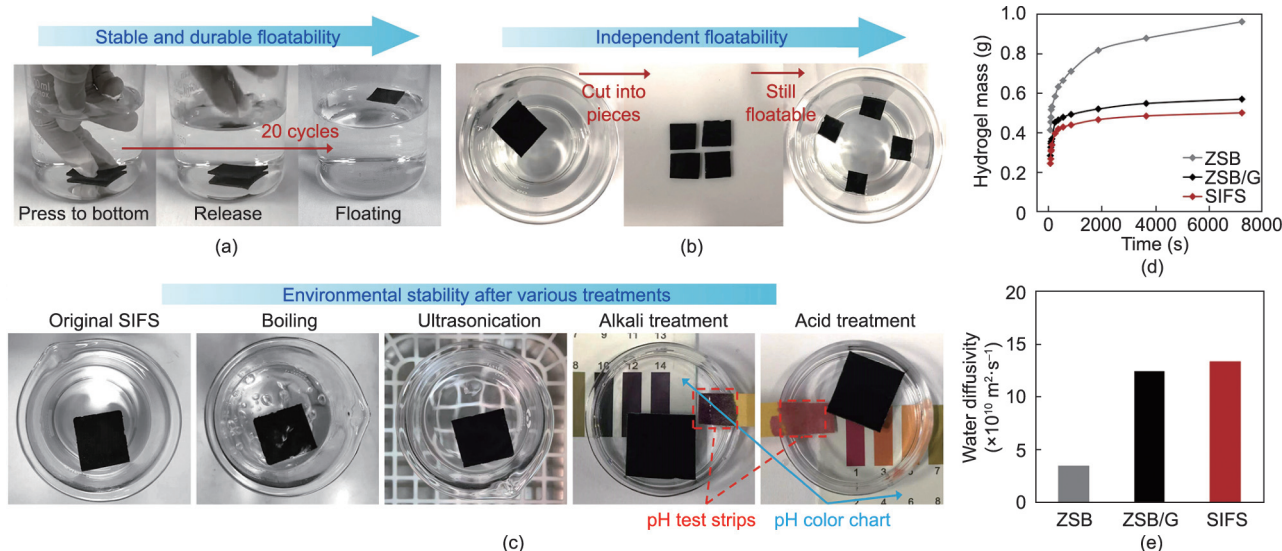


**Fig. 2.** Durable and independent self-floating of the SIFS evaporator. (a) Cyclic compression test demonstrated the stable and durable self-floating ability of the SIFS evaporator. (b) The SIFS evaporator possessed independent self-floating since it still floated after being cut into pieces. (c) The SIFS evaporator can keep mechanically and chemically stable towards complex environments, such as 1 h each for boiling, ultrasonication, alkali and acidic treatments. (d) Mass change of hydrogel samples in 3.6 wt% NaCl. (e) Water diffusivity.

$$D_w = \frac{\pi l^2}{16} \left[ \frac{d(M_t/M_\infty)}{d(t^{1/2})} \right]^2 \tag{3}$$

where $D_w$ is the water diffusivity, $l$ is the thickness of the SIFS hydrogel, $M_t$ represents the weight of absorbed water at time $t$, $M_\infty$ represents the final weight of absorbed water, and $d(M_t/M_\infty)/d(t^{1/2})$ is the slope of the linear portion of $M_t/M_\infty$ as a function of $t^{1/2}$ in the region of $M_t/M_\infty < 0.60$ (60% saturated water absorption) [62]. Pure ZSB reached 60% saturated water absorption at 786 s, corresponding to a water diffusivity of $3.59 \times 10^{-10}$ m²·s⁻¹. While ZSB/G and SIFS samples reached the same stage much more rapidly in 226 and 211 s, corresponding to water diffusivities of $1.250 \times 10^{-9}$ and $1.339 \times 10^{-9}$ m²·s⁻¹, respectively (Fig. S8 and

Tables S1 and S2 in Appendix A). In addition, the prominently enhanced water diffusion indicates the interconnect channels inside the SIFS sheets. In addition, a piece of dry filter paper was applied to the SIFS surface to visually exhibit the water transport (Fig. S9 and Video S5 in Appendix A). The filter paper was fully permeated the moment it contacted the SIFS surface, confirming the presence of the water film induced by superhydrophilic ZSB, and the fluent water transport inside the SIFS floater. These results demonstrated that hydrogels containing HGBs exhibited significantly faster water uptake, while CB did not affect this. Combined with the cross-sectional morphology of the SIFS samples in Fig. 1(c), it can be concluded that densely packed HGBs left plenty of interstices and holes due to their spherical surfaces. These holes were connected to each

other to build a porous structure and reticulated microchannels for water transport. Thus, HGB-containing ZSB/G and SIFS hydrogels possessed significantly higher water diffusivities that were 3.48 and 3.72 times that of the pure ZSB hydrogel, respectively.

### 3.3. Solar desalination performance

Carbon-based substrates such as CB nanoparticles and graphene oxide possess excellent solar absorption and photothermal conversion properties owing to the optical transitions of π bands [63]. The SIFS evaporator doped with CB nanoparticles exhibited broadband solar absorption of 96.35% and low reflection of 1.83% (Fig. 3(a) and Appendix A Fig. S10), as compared to ZSB (50.13% for absorption and 25.38% for reflection) and ZSB/G (78% for absorption and 10.92% for reflection). The CB was embedded in the ZSB of the SIFS sheet, and because of ZSB gel encapsulation, the nanostructure on CB could not be observed (Fig. S11 in Appendix A). A controlled experiment was performed to calculate the actual equivalent enthalpy (Fig. S12 in Appendix A) for the evaporators [64]. ZSB/G and SIFS hydrogels with thicknesses ranging from 1 to 5 mm were employed to perform the evaporation test using a solar simulator (SOLAR-500, NBeT, China) with an AM 1.5G light filter and a xenon lamp. According to Figs. 3(b)–(d), higher water evaporation rate, surface temperature, and photothermal conversion efficiency could be observed on thicker floaters owing to better heat insulation. During this period, the SIFS floaters reached a steady state with a maximum steam generation rate of 1.35 kg·m$^{-2}$·h$^{-1}$ and a conversion efficiency of 63.27% under 1 sun intensity (1 kW·m$^{-2}$), compared with previous works (Table S3 in Appendix A). In comparison, the evaporation rate of pure water is only 0.11 kg·m$^{-2}$·h$^{-1}$. For control ZSB/G floaters, the maximum evaporation rate was calculated to be 0.50 kg·m$^{-2}$·h$^{-1}$ under the same light density, which was 63% lower than that of SIFS sample because of the lack of photothermal conversion composition. The conversion efficiency ($\eta$) can be defined and calculated according to Eq. (4) [65]:

$$\eta = \frac{m(C_p \times \Delta T + \Delta H_{vap})}{C_{opt}I} \qquad (4)$$

where $m$ is the water evaporation rate, $C_p$ is the specific heat capacity of water, $\Delta T$ is the temperature difference between the vapor and ambient, and $\Delta H_{vap}$ represents the enthalpy of water evaporation calculated from the controlled experiment described in Section S1.2 in Appendix A. $C_{opt}$ is the optical concentration, and $I$ refers to solar irradiation intensity of 1 sun. The water evaporation enthalpy of SIFS is lower than that of bulk water, which may be explained by "water cluster theory" [66,67]. Water can be evaporated as individual molecules or clusters containing several molecules. When water evaporates from the polymer gel network, it is more likely to escape as clusters than single molecules. Therefore, the water in the SIFS exhibits a lower actual evaporation enthalpy than the conventional latent heat [68].

The surface temperature of the 5 mm SIFS evaporator during 300 min of irradiation was recorded by an infrared camera, as shown in Appendix A Fig. S13. The temperature was increased from 19.4 to 28.1 °C in 5 min, and finally reached 51.6 °C after 300 min illumination. COMSOL Multiphysics software (COMSOL, Sweden) was used to simulate the heat transfer and temperature distribution around the SIFS evaporator floating at the air/water interface (Fig. 3(e)). The top 28% of the floater was exposed to air, and the bottom 72% was immersed in bulk water, corresponding to its density. The temperature difference between HGB and ZSB was balanced within a few milliseconds; thus, the SIFS floater exhibited a reduced homogeneous heat transfer performance compared with the pure ZSB hydrogel (see more details in Appendix A Fig. S14).

Effective decontamination ability and long-term stability are highly desired in seawater desalination for real-world applications. The water quality before and after desalination was evaluated using inductively coupled plasma mass spectrometry (ICP–MS, 7700x, Agilent, USA). After evaporation and condensation processes, the concentrations of four primary ions, Na$^+$, Mg$^{2+}$, K$^+$, and Ca$^{2+}$, were sharply reduced and were significantly lower than the values suggested by the World Health Organization (WHO) (Fig. 3(f)) [69]. Various artificial wastewater samples, including artificial industrial wastewater (AIW), artificial domestic wastewater (ADW), artificial oily wastewater (AOW), artificial medical
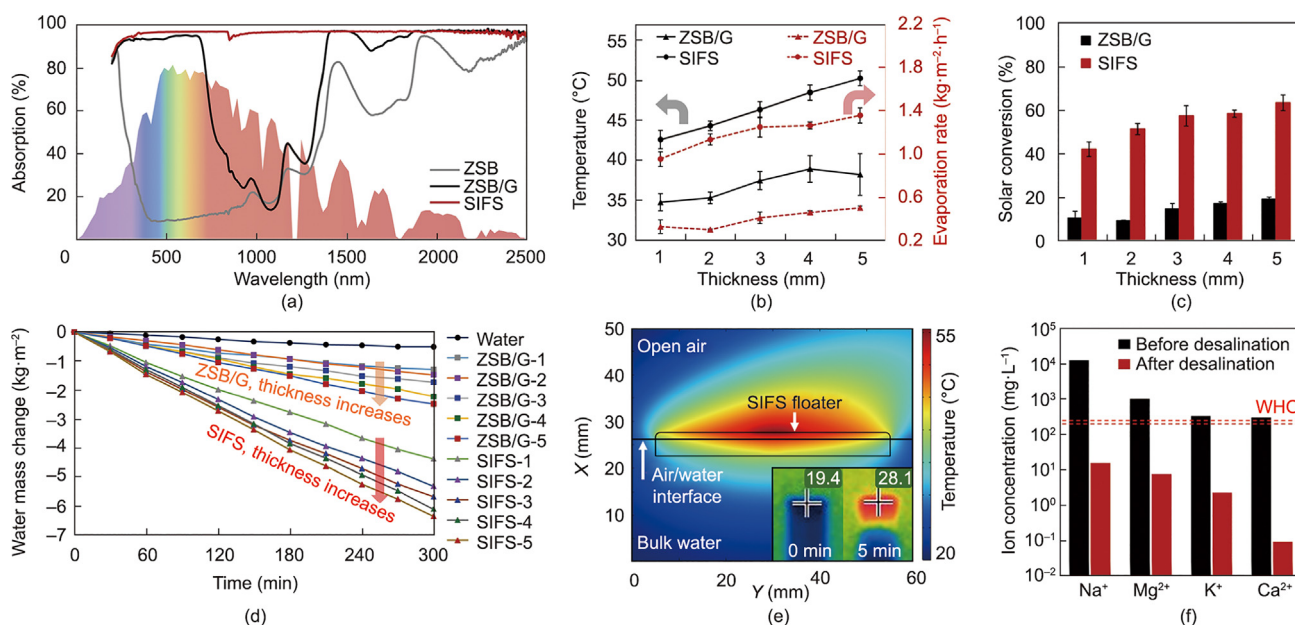


**Fig. 3.** Solar evaporation performance of the SIFS evaporator. (a) Solar absorption spectra of the SIFS evaporator with an average absorption of 96.35%. (b) Water evaporation rate and surface temperature with different thickness (1, 2, 3, 4, and 5 mm) of ZSB/G and SIFS samples under 1 sun during 300 min illumination. (c) Solar conversion efficiency vs thickness. (d) The water mass change vs time. (e) COMSOL simulated temperature distribution of a 5 mm SIFS evaporator floating at the air/water interface and the infrared images of 5 mm SIFS evaporator under 1 sun (bottom right). (f) Concentrations of primary ions before and after solar desalination via the SIFS evaporator.

wastewater (AMW), and artificial printing and dyeing wastewater (APW), were prepared and applied to SIFS evaporators to simulate practical working conditions. In 30 day tests, the SIFS evaporators maintained an intact structure without leakage or degradation (Fig. S15 in Appendix A). These results demonstrated that the SIFS evaporator could deliver purified water far above the WHO standards and performing long-term desalination in seawater and wastewater.
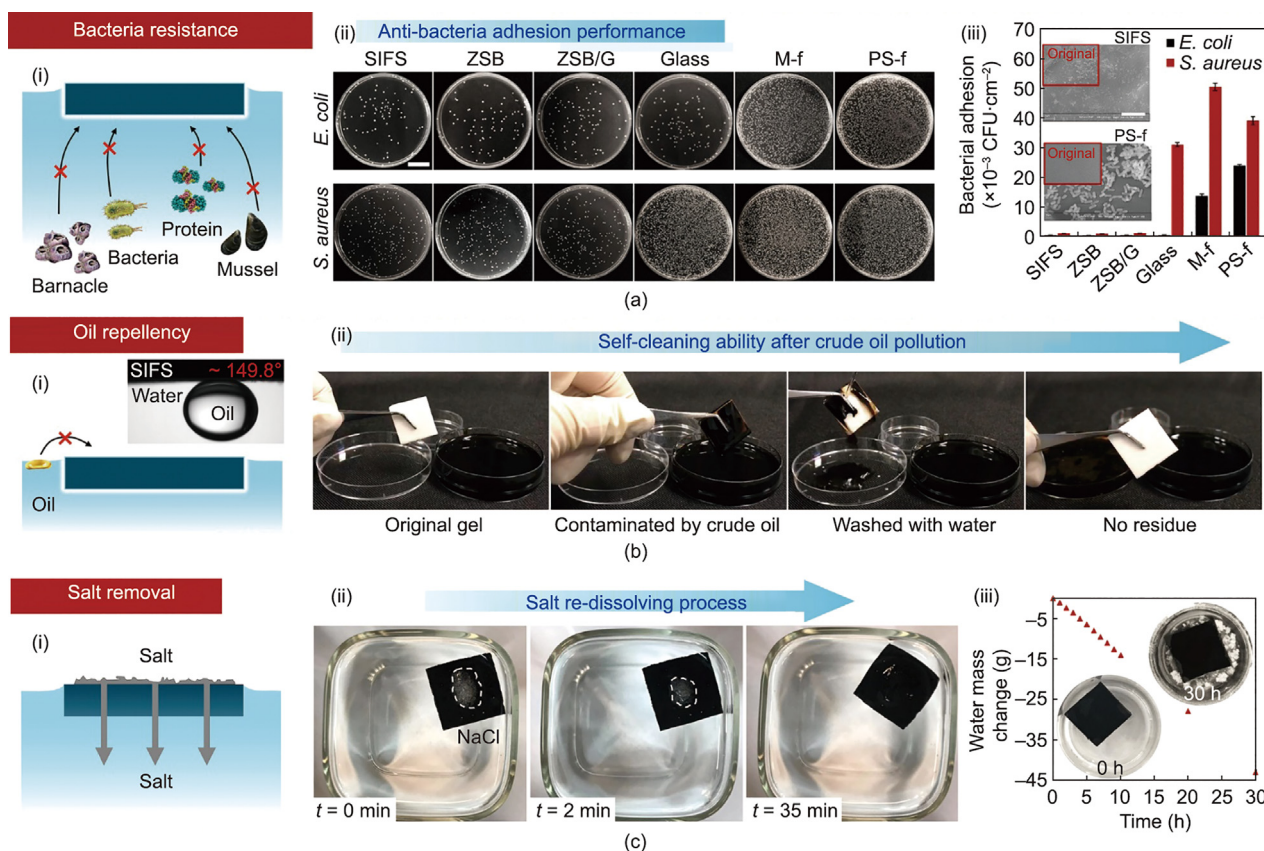
### 3.4. Multi-contamination resistance

Salt accumulation during solar steam generation strongly affects the performance and long-term robustness of evaporators. A useful strategy to achieve salt rejection is rapid redissolution of the deposited salt on the evaporator. Meanwhile, evaporators with superhydrophilicity possess the capacity to repel oil- and biofoulants. Zwitterionic materials are characterized by high dipole moments and contain strongly charged groups; yet, they are overall charge neutral [70]. Because of the ionic groups, zwitterion materials can bind water molecules via ionic solvation to form a hydration layer and exhibit superhydrophilicity. The highly hydrophilic surface can be fully wetted to provide a continuous and stable water supply, further redissolving the deposited salt back into the sea [71]. More importantly, from a thermodynamic point of view, it would cost a large amount of energy for various foulants to pass through the hydration layer. The maximum Gibbs free energy of zwitterionic functionalized surfaces is extremely high, thus fouling is not prone to occur [72].

The anti-biofouling properties of the SIFS evaporator were investigated by protein adsorption and bacterial adhesion assays. FITC-BSA was used for the protein adsorption test (Fig. S16 in Appendix A). Two species of bacteria, Gram-negative *E. coli* and Gram-positive *S. aureus*, were selected for the anti-bacterial assessment. PS-f and melamine foam (M-f) were used as controls. As shown in Fig. 4(a), after 2 h co-incubation, PS-f and M-f were severely polluted by both *E. coli* and *S. aureus*. PS-f, the most used heat insulator in previous studies, was contaminated with bacterial densities of $2.391 \times 10^4$ colony-forming units (CFU)·cm$^{-2}$ for *E. coli* and $3.896 \times 10^4$ CFU·cm$^{-2}$ for *S. aureus*. In contrast, the zwitterion-based SIFS hydrogel showed remarkable bacterial repellence, corresponding to 97.93% and 97.00% reductions for *E. coli* and *S. aureus* adhesion, respectively, compared with PS-f. SEM images of samples that were co-cultured with *E. coli* for 3 d showed severe bacterial contamination on PS-f (Fig. 4(a) and Appendix A Fig. S17). In sharp contrast, no bacterial colonies visibly adhered to the SIFS surface.

The SIFS hydrogel was used in the contact angle test, and the ZSB/G hydrogel was assessed with an oil removal test for better visual perception. Crude oil and soybean oil were selected for the tests, as shown in Fig. 4(b) and Appendix A Fig. S18. When completely wetted, a water film surrounded the SIFS hydrogel. The contact angle of an oil droplet on the SIFS surface under water, $\theta_{OW}$, can be expressed using Eq. (5) [73]:

$$\cos\theta_{OW} = \frac{\gamma_{OA}\cos\theta_O - \gamma_{WA}\cos\theta_W}{\gamma_{OW}} \tag{5}$$



**Fig. 4.** Multi-contamination resistance of the SIFS evaporator. (a-i) Illustration of bacterial resistance of SIFS hydrogel. The ionic solvation effect-induced hydration layer of ZSB hydrogel protects the SIFS evaporator from bio-foulant adhesion. (a-ii) Optical photographs (scale bar: 2 cm). (a-iii) The normalized bacterial adhesion and SEM images after *E. coli* and *S. aureus* contamination on various samples (scale bar: 5 μm). (b-i) Schematic of oil repellence of SIFS hydrogel with underwater superoleophobicity. (b-ii) Self-cleaning property of ZSB/G (SIFS hydrogel without CB) after crude oil contamination. ZSB/G was used for better visual perception of oil removal. (c-i) Illustration of salt removal on the SIFS hydrogel. (c-ii) The salt that manually applied to the SIFS hydrogel was gradually dissolved into 3.6 wt% NaCl solution. (c-iii) SIFS hydrogel was able to constantly vaporize the underlying water into steam for 30 h without being blocked.

where $\gamma_{OA}$, $\gamma_{WA}$, and $\gamma_{OW}$ represent the surface tensions of the oil/air, water/air, and oil/water interfaces, respectively; $_O$ and $_W$ are the oil contact angle and water contact angle of the surface, respectively. For the SIFS hydrogel, an superhydrophilic material, $\gamma_{OA} \cos \theta_O$ is generally lower than $\gamma_{WA} \cos \theta_W$. Because $\gamma_{OA}$ is significantly lower than $\gamma_{WA}$, $\cos \theta_O$ and $\cos \theta_W$ are both greater than 0 and less than 1. Thus, the value of $\cos \theta_{OW}$ is negative, indicating an underwater oleophobicity of the SIFS hydrogel, which is consistent with Fig. 4(b). Therefore, oil repellence guaranteed SIFS self-cleaning. Even if immersed in crude oil, it should recover its previous clean state with a simple rinse (Videos S6–S8 in Appendix A).

The salt resistance of the SIFS hydrogel was evaluated by tests for salt redissolution, degradation, absorption, and long-term evaporation. In the redissolution test, salt was directly sprinkled on a floating SIFS evaporator, and because of the water film induced by ZSB molecules, salt was immediately wetted and gradually redissolved into the bulk water (Fig. 4(c)). In the degradation test, the SIFS hydrogel was proved to possess salt-rejection properties, as it could maintain a stable swelling ratio through five cycles (Fig. S19 in Appendix A). In the absorption test, the high salt resistance ratio of the SIFS evaporator (88.16%) was mainly due to the high size stability and low swelling ratio (Fig. S20 in Appendix A). The long-term salt resistance was also assessed. The SIFS evaporator was floated in 3.6 wt% NaCl solution to proceed with stable steam generation. After 30 h illumination, no salt sediments were deposited on the SIFS evaporator, while a large amount of salt was crystallized at the bottom of the beaker (Fig. 4(c)). These results demonstrated that, in salt solution as the SIFS evaporator avoided degradation and crystallization, it was capable of performing highly stable and durable solar desalination in practical applications. Therefore, the zwitterion-based fully superhydrophilic SIFS evaporator successfully achieved multi-contamination resistance, including salt accumulation, oil pollution, microbial adhesion, and protein adsorption.

### 3.5. Wastewater purification and outdoor experiment

Universal solution processing capacity is desired in an ideal solar interfacial evaporation system, which enables high-efficiency purification and long-term durability in various types of wastewater. Owing to the prominent chemical stability and multi-contamination resistance of fully superhydrophilic materials, water evaporation from complex solutions can be achieved via the SIFS floater. Artificial wastewater samples were used for the purification assays (Fig. 5(a)). SIFS evaporators (5 cm × 5 cm in size) were floated on each type of wastewater. After 300 min illumination, the water mass change was recorded as a function of time, as shown in Fig. 5(b). SIFSs in APW and ADW exhibited evaporation performance similar to that of artificial seawater, while the evaporation rates of SIFSs in AOW, AMW, and AIW slightly decreased, which may be ascribed to the diffusion of oil and the increase in solution viscosity. The absorption spectra of the wastewater samples before and after purification were shown in Appendix A Fig. S21. The original wastewater exhibited strong absorption in the detection range, while the spectra of wastewater were similar to those of DI with no obvious absorption signals after purification. An *in vitro* cell proliferation test was performed to assess the cytotoxicity of various water samples, including lixivia of ZSB, ZSB/G, and SIFS hydrogels (L-ZSB, L-ZSB/G, and L-SIFS), evaporated water (EW) purified with an SIFS evaporator, and the original AIW, ADW, AOW, AMW, and APW. DI with a resistance of 18.20 MΩ·cm$^{-1}$ was chosen as the control. As shown in Fig. 5(c), significant reductions in cell viability were observed in wastewater-treated cells than in DI-treated cells. In particular, the AIW and AOW groups showed cell viabilities of 23.48% and 21.79%, respectively. Wastewater is a complex system that may contain harmful components, such as heavy metal ions, which can be toxic as they damage nerves, livers, bones, and other organs; heavy metals can also inhibit the functionality of vital enzymes [74]. Meanwhile, the cell viabilities of L-ZSB, L-ZSB/G, L-SIFS, and EW showed negligible differences compared to that in DI. The results demonstrated that the SIFS evaporator was nontoxic and safe, and it was capable of producing clean water from various conditions without damaging the original source.

The outdoor experiment was conducted in Tianjin University, Jinnan District, Tianjin, China, in December (i.e., winter). The solar flux there was 200–1000 W·m$^{-2}$ at that time on sunny days, with the air temperature ranging from −5 to 10 °C and humidity from
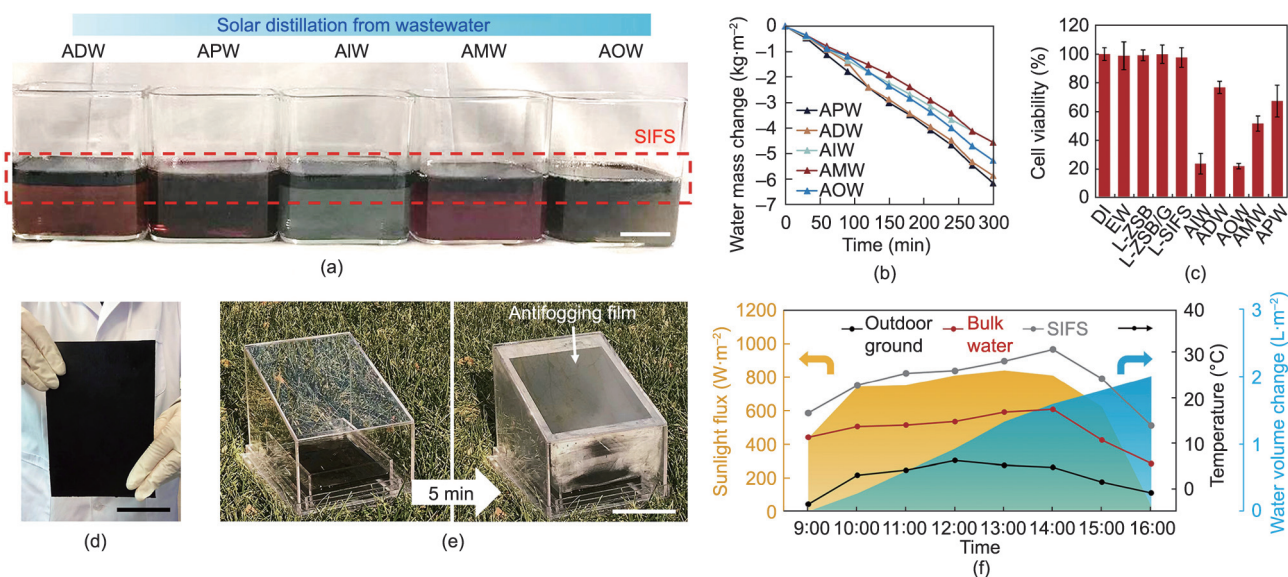


**Fig. 5.** Wastewater purification and outdoor evaporation tests of the SIFS evaporator under natural sunlight. Various liquids were used in the purifying tests, i.e., DI, lixiviums of ZSB, ZSB/G, and SIFS hydrogels (L-ZSB, L-ZSB/G, and L-SIFS, respectively), EW after desalination with SIFS evaporator, AIW, ADW, AOW, AMW, and APW. (a) Optical images of various artificial wastewater samples before purification (scale bar: 2 cm). (b) Water mass change during wastewater purification versus time. (c) Cytotoxicity evaluation of purified wastewater samples from cell viability. (d) Optical image of the SIFS evaporator used in the outdoor test (scale bar: 5 cm). (e) Steam generation occurred within 5 min under natural illumination. (f) The solar flux, water volume change, temperatures of outdoor ground, bulk water, and SIFS evaporator during the outdoor experiment.

20% to 40% during the daytime. An SIFS floater with a size of 10 cm × 15 cm was used to perform the test, as shown in Fig. 5(d). The solar flux was absorbed by the SIFS evaporator and converted into thermal energy to heat water, and then steam was generated. The cap provided an enclosed space for evaporation and worked as the cold end to condense the steam (a commercial antifogging film was employed to reduce the incident light loss). Water droplets could be observed on the wall of the cap 5 min after the device was deployed in sunlight (Fig. 5(e)). The mass change of the collected water, the temperatures of the SIFS evaporator, bulk water, and outdoor ground versus time were all recorded in Fig. 5(f). The temperature of the SIFS surface increased by 14.3 °C (from 16.9 to 31.2 °C) with increasing sunlight flux and decreased due to sunset. The maximum temperature was lower than that in the indoor test (51.6 °C), which was probably attributed to the cold conditions and strong winds in winter. During this period, the bulk water temperature was 5.5–13.5 °C lower than that of the SIFS surface. After 7 h evaporation, this device collected ∼30 mL of clean water, corresponding to a collection rate of ∼2 L·m$^{-2}$, showing its potential to produce freshwater for human demands.

## 4. Conclusions

In conclusion, inspired by the gas-vesicle structure of seaweeds, we have developed a fully superhydrophilic but independently floatable SIFS evaporator via a facile method. ZSB, HGBs, and CB were integrated to achieve durable and stable solar desalination for long-term practical applications. The densely packed HGBs in the SIFS evaporator enabled low density and heat insulation, allowing it to perform interfacial evaporation even if it was fully wetted or torn into pieces during storm events. CB with broadband light absorption and photothermal conversion was selected as the solar absorber, thereby ensuring that the SIFS evaporator only consumed inexhaustible solar energy and abundant seawater to produce freshwater. The ZSB gel played an indispensable role as a hydrophilic adhesive. More importantly, because of the hydration layer induced by ZSB via ionic solvation effects, the SIFS evaporator exhibited superhydrophilicity and multi-contamination resistance. The superhydrophilic SIFS evaporator was fully wetted when floating on water; subsequently, continuous water pumping dissolved salt deposits and provided uninterrupted water supply, endowing the SIFS evaporator with stable steam generation and salt rejection. The hydration layer also worked as a shield to inhibit oil- and biofoulant adhesion, protecting the SIFS evaporator from oil pollution and microbiological corrosion. Owing to the collective properties of broadband light absorption, heat insulation, independent floating, continuous water pumping, salt rejection, oil repellence, and biofouling inhibition, an optimized water evaporation rate of 1.35 kg·m$^{-2}$·h$^{-1}$ was achieved with 63.27% photothermal conversion. With long-term stability and robustness, the SIFS evaporator provides a sustainable and eco-friendly strategy for harnessing inexhaustible solar energy to fulfill the ever-increasing freshwater demands of the society.

## Acknowledgments

## Compliance with ethical guidelines

## Appendix A. Supplementary data

Supplementary data to this article can be found online at https://doi.org/10.1016/j.eng.2021.06.029.

## References

[1] Elimelech M, Phillip WA. The future of seawater desalination: energy, technology, and the environment. Science 2011;333(6043):712–7.

[2] Gao M, Zhu L, Peh CK, Ho GW. Solar absorber material and system designs for photothermal water vaporization towards clean water and energy production. Energy Environ Sci 2019;12(3):841–64.

[3] Wu X, Gao T, Han C, Xu J, Owens G, Xu H. A photothermal reservoir for highly efficient solar steam generation without bulk water. Sci Bull 2019;64(21):1625–33.

[4] Zhu L, Gao M, Peh CK, Ho GW. Solar-driven photothermal nanostructured materials designs and prerequisites for evaporation and catalysis applications. Mater Horiz 2018;5(3):323–43.

[5] Zhang Y, Ravi SK, Tan SC. Food-derived carbonaceous materials for solar desalination and thermo-electric power generation. Nano Energy 2019;65:104006.

[6] Wang Y, Wu X, Shao B, Yang X, Owens G, Xu H. Boosting solar steam generation by structure enhanced energy management. Sci Bull 2020;65(16):1380–8.

[7] Hu X, Zhu J. Tailoring aerogels and related 3D macroporous monoliths for interfacial solar vapor generation. Adv Funct Mater 2020;30(3):1907234.

[8] Ni F, Qiu N, Xiao P, Zhang C, Jian Y, Liang Y, et al. Tillandsia-inspired hygroscopic photothermal organogels for efficient atmospheric water harvesting. Angew Chem Int Ed Engl 2020;59(43):19237–46.

[9] Xu Z, Zhang L, Zhao L, Li B, Bhatia B, Wang C, et al. Ultrahigh-efficiency desalination via a thermally-localized multistage solar still. Energy Environ Sci 2020;13(3):830–9.

[10] Kim H, Yang S, Rao SR, Narayanan S, Kapustin EA, Furukawa H, et al. Water harvesting from air with metal–organic frameworks powered by natural sunlight. Science 2017;356(6336):430–4.

[11] Li T, Liu H, Zhao X, Chen G, Dai J, Pastel G, et al. Scalable and highly efficient mesoporous wood-based solar steam generation device: localized heat, rapid water transport. Adv Funct Mater 2018;28(16):1707134.

[12] Jiang M, Shen Q, Zhang J, An S, Ma S, Tao P, et al. Bioinspired temperature regulation in interfacial evaporation. Adv Funct Mater 2020;30(14):1910481.

[13] Ghasemi H, Ni G, Marconnet AM, Loomis J, Yerci S, Miljkovic N, et al. Solar steam generation by heat localization. Nat Commun 2014;5(1):4449.

[14] Shi L, Shi Y, Zhuo S, Zhang C, Aldrees Y, Aleid S, et al. Multi-functional 3D honeycomb ceramic plate for clean water production by heterogeneous photo-Fenton reaction and solar-driven water evaporation. Nano Energy 2019;60:222–30.

[15] Ge J, Zong D, Jin Q, Yu J, Ding B. Biomimetic and superwettable nanofibrous skins for highly efficient separation of oil-in-water emulsions. Adv Funct Mater 2018;28(10):1705051.

[16] Yao Y, Lv T, Li N, Chen Z, Zhang C, Chen T. Selected functionalization of continuous graphene fibers for integrated energy conversion and storage. Sci Bull 2020;65(6):486–95.

[17] Zhao F, Guo Y, Zhou X, Shi W, Yu G. Materials for solar-powered water evaporation. Nat Rev Mater 2020;5(5):388–401.

[18] Gao B, Nakano S, Harada H, Miyamura Y, Sekiguchi T, Kakimoto K. Single-seed casting large-size monocrystalline silicon for high-efficiency and low-cost solar cells. Engineering 2015;1(3):378–83.

[19] Nandakumar DK, Ravi SK, Zhang Y, Guo N, Zhang C, Tan SC. A super hygroscopic hydrogel for harnessing ambient humidity for energy conservation and harvesting. Energy Environ Sci 2018;11(8):2179–87.

[20] Liang H, Liao Q, Chen N, Liang Y, Lv G, Zhang P, et al. Thermal efficiency of solar steam generation approaching 100% through capillary water transport. Angew Chem Int Ed Engl 2019;58(52):19041–6.

[21] Xiao M, Wang S, Thaweesak S, Luo B, Wang L. Tantalum (oxy)nitride: narrow bandgap photocatalysts for solar hydrogen generation. Engineering 2017;3(3):365–78.

[22] Zhang Y, Ravi SK, Vaghasiya JV, Tan SC. A barbeque-analog route to carbonize moldy bread for efficient steam generation. iScience 2018;3:31–9.

[23] Hu X, Xu W, Zhou L, Tan Y, Wang Y, Zhu S, et al. Tailoring graphene oxide-based aerogels for efficient solar steam generation under one sun. Adv Mater 2017;29(5):1604031.

[24] Zhang B, Song C, Liu C, Min J, Azadmanjiri J, Ni Y, et al. Molten salts promoting the "controlled carbonization" of waste polyesters into hierarchically porous carbon for high-performance solar steam evaporation. J Mater Chem A 2019;7 (40):22912–23.

[25] Yang M, Schäffler R, Repmann T, Orgassa K. Moisture absorption and desorption in an ionomer-based encapsulant: a type of self-breathing encapsulant for CIGS thin-film PV modules. Engineering 2020;6(12):1403–7.

[26] Huang Q, Jiang F, Wang L, Yang C. Design of photobioreactors for mass cultivation of photosynthetic organisms. Engineering 2017;3(3):318–29.

[27] Chen C, Kuang Y, Hu L. Challenges and opportunities for solar evaporation. Joule 2019;3(3):683–718.

[28] Liu H, Huang Z, Liu K, Hu X, Zhou J. Interfacial solar-to-heat conversion for desalination. Adv Energy Mater 2019;9(21):1900310.

[29] Zhang C, Liang HQ, Xu ZK, Wang Z. Harnessing solar-driven photothermal effect toward the water–energy nexus. Adv Sci 2019;6(18):1900883.

[30] Zhang P, Li J, Lv L, Zhao Y, Qu L. Vertically aligned graphene sheets membrane for highly efficient solar thermal generation of clean water. ACS Nano 2017;11 (5):5087–93.

[31] He J, Zhang Z, Xiao C, Liu F, Sun H, Zhu Z, et al. High-performance salt-rejecting and cost-effective superhydrophilic porous monolithic polymer foam for solar steam generation. ACS Appl Mater Interfaces 2020;12(14):16308–18.

[32] Wang F, Hu Z, Fan Y, Bai W, Wu S, Sun H, et al. Salt-rejection solar absorbers based on porous ionic polymers nanowires for desalination. Macromol Rapid Commun 2021;42(4):2000536.

[33] Ling N, Forsythe S, Wu Q, Ding Y, Zhang J, Zeng H. Insights into *Cronobacter sakazakii* biofilm formation and control strategies in the food industry. Engineering 2020;6(4):393–405.

[34] He J, Fan Y, Xiao C, Liu F, Sun H, Zhu Z, et al. Enhanced solar steam generation of hydrogel composite with aligned channel and shape memory behavior. Compos Sci Technol 2021;204:108633.

[35] Dong Y, Wu ZS, Ren W, Cheng HM, Bao X. Graphene: a promising 2D material for electrochemical energy storage. Sci Bull 2017;62(10):724–40.

[36] Han N, Liu K, Zhang X, Wang M, Du P, Huang Z, et al. Highly efficient and stable solar-powered desalination by tungsten carbide nanoarray film with sandwich wettability. Sci Bull 2019;64(6):391–9.

[37] Ni G, Zandavi SH, Javid SM, Boriskina SV, Cooper TA, Chen G. A salt-rejecting floating solar still for low-cost desalination. Energy Environ Sci 2018;11 (6):1510–9.

[38] Xu N, Zhu P, Sheng Y, Zhou L, Li X, Tan H, et al. Synergistic tandem solar electricity–water generators. Joule 2020;4(2):347–58.

[39] Zeng Y, Yao J, Horri BA, Wang K, Wu Y, Li D, et al. Solar evaporation enhancement using floating light-absorbing magnetic particles. Energy Environ Sci 2011;4(10):4074.

[40] Sun C, Wen B, Bai B. Recent advances in nanoporous graphene membrane for gas separation and water purification. Sci Bull 2015;60(21):1807–23.

[41] Li R, Zhang L, Shi L, Wang P. MXene Ti3C2: an effective 2D light-to-heat conversion material. ACS Nano 2017;11(4):3752–9.

[42] Xu N, Li J, Wang Y, Fang C, Li X, Wang Y, et al. A water lily-inspired hierarchical design for stable and efficient solar evaporation of high-salinity brine. Sci Adv 2019;5(7):aaw7013.

[43] Ni G, Li G, Boriskina SV, Li H, Yang W, Zhang T, et al. Steam generation under one sun enabled by a floating structure with thermal concentration. Nat Energy 2016;1(9):16126.

[44] Kane IA, Clare MA, Miramontes E, Wogelius R, Rothwell JJ, Garreau P, et al. Seafloor microplastic hotspots controlled by deep-sea circulation. Science 2020;368(6495):1140–5.

[45] Tao P, Ni G, Song C, Shang W, Wu J, Zhu J, et al. Solar-driven interfacial evaporation. Nat Energy 2018;3(12):1031–41.

[46] Guo Y, Zhou X, Zhao F, Bae J, Rosenberger B, Yu G. Synergistic energy nanoconfinement and water activation in hydrogels for efficient solar water desalination. ACS Nano 2019;13(7):7913–9.

[47] Walsby AE, Booker MJ. Changes in buoyancy of a planktonic blue-green alga in response to light intensity. Br Phycol J 1980;15(4):311–9.

[48] Bowen CC, Jensen TE. Blue-green algae: fine structure of the gas vacuoles. Science 1965;147(3664):1460–2.

[49] Cohen-Bazire G, Kunisawa R, Pfennig N. Comparative study of the structure of gas vacuoles. J Bacteriol 1969;100(2):1049–61.

[50] Zhao Y, Yu C, Lan H, Cao M, Jiang L. Improved interfacial floatability of superhydrophobic/superhydrophilic Janus sheet inspired by lotus leaf. Adv Funct Mater 2017;27(27):1701466.

[51] Geng H, Bai H, Fan Y, Wang S, Ba T, Yu C, et al. Unidirectional water delivery on a superhydrophilic surface with two-dimensional asymmetrical wettability barriers. Mater Horiz 2018;5(2):303–8.

[52] Wen C, Guo H, Bai H, Xu T, Liu M, Yang J, et al. Beetle-inspired hierarchical antibacterial interface for reliable fog harvesting. ACS Appl Mater Interfaces 2019;11(37):34330–7.

[53] Zhang L, Cao Z, Bai T, Carr L, Ella-Menye JR, Irvin C, et al. Zwitterionic hydrogels implanted in mice resist the foreign-body reaction. Nat Biotechnol 2013;31 (6):553–6.

[54] Phiri I, Eum KY, Kim JW, Choi WS, Kim SH, Ko JM, et al. Simultaneous complementary oil–water separation and water desalination using functionalized woven glass fiber membranes. J Ind Eng Chem 2019;73:78–86.

[55] Prakash I, Muralidharan P, Nallamuthu N, Satyanarayana N, Venkateswarlu M, Carnahan D. Preparation of NiAl2O4/SiO2 and Co2+-doped NiAl2O4/SiO2 nanocomposites by the sol–gel route. J Am Ceram Soc 2006;89(7):2220–5.

[56] Prakash I, Nallamuthu N, Muralidharan P, Venkateswarlu M, Satyanarayana N. Synthesis of SiO2/CoFe2O4 nanocomposite by base catalyst assisted *in-situ* sol–gel process. AIP Conf Proc 2010;1276(1):227–32.

[57] Cai Y, Lu Q, Guo X, Wang S, Qiao J, Jiang L. Salt-tolerant superoleophobicity on alginate gel surfaces inspired by seaweed (*Saccharina japonica*). Adv Mater 2015;27(28):4162–8.

[58] He K, Duan H, Chen GY, Liu X, Yang W, Wang D. Cleaning of oil fouling with water enabled by zwitterionic polyelectrolyte coatings: overcoming the imperative challenge of oil–water separation membranes. ACS Nano 2015;9 (9):9188–98.

[59] Li C, Jiang D, Huo B, Ding M, Huang C, Jia D, et al. Scalable and robust bilayer polymer foams for highly efficient and stable solar desalination. Nano Energy 2019;60:841–9.

[60] Hogan NJ, Urban AS, Ayala-Orozco C, Pimpinelli A, Nordlander P, Halas NJ. Nanoparticles heat through light localization. Nano Lett 2014;14(8):4640–5.

[61] Wang JH. Self-diffusion coefficients of water. J Phys Chem 1965;69(12):4412.

[62] Zeng J, Wang Q, Shi Y, Liu P, Chen R. Osmotic pumping and salt rejection by polyelectrolyte hydrogel for continuous solar desalination. Adv Energy Mater 2019;9(38):1900552.

[63] Liu G, Xu J, Wang K. Solar water evaporation by black photothermal sheets. Nano Energy 2017;41:269–84.

[64] Guo Y, Zhao F, Zhou X, Chen Z, Yu G. Tailoring nanoscale surface topography of hydrogel for efficient solar vapor generation. Nano Lett 2019;19(4):2530–6.

[65] Zhou J, Gu Y, Liu P, Wang P, Miao L, Liu J, et al. Development and evolution of the system structure for highly efficient solar steam generation from zero to three dimensions. Adv Funct Mater 2019;29(50):1903255.

[66] Miyazaki M, Fujii A, Ebata T, Mikami N. Infrared spectroscopic evidence for protonated water clusters forming nanoscale cages. Science 2004;304 (5674):1134–7.

[67] Fujii A, Mizuse K. Infrared spectroscopic studies on hydrogen-bonded water networks in gas phase clusters. Int Rev Phys Chem 2013;32(2):266–307.

[68] Zhao F, Zhou X, Shi Y, Qian X, Alexander M, Zhao X, et al. Highly efficient solar vapour generation via hierarchically nanostructured gels. Nat Nanotechnol 2018;13(6):489–95.

[69] World Health Organization. Guidelines for drinking-water quality. 4th ed. Geneva: World Health Organization; 2011.

[70] Shao Q, Jiang S. Molecular understanding and design of zwitterionic materials. Adv Mater 2015;27(1):15–26.

[71] Mu P, Zhang Z, Bai W, He J, Sun H, Zhu Z, et al. Superwetting monolithic hollow-carbon-nanotubes aerogels with hierarchically nanoporous structure for efficient solar steam generation. Adv Energy Mater 2019;9(1):1802158.

[72] Wei Q, Becherer T, Angioletti-Uberti S, Dzubiella J, Wischke C, Neffe AT, et al. Protein interactions with polymer coatings and biomaterials. Angew Chem Int Ed Engl 2014;53(31):8004–31.

[73] Jung YC, Bhushan B. Wetting behavior of water and oil droplets in three-phase interfaces for hydrophobicity/philicity and oleophobicity/philicity. Langmuir 2009;25(24):14165–73.

[74] Malik A. Metal bioremediation through growing cells. Environ Int 2004;30 (2):261–78.